Numerical simulation of bluff body turbulent flows using hybrid RANS/LES turbulence models

Ricardo Franco, Cesar Celis, Luís Fernando Figueira da Silva

Numerical simulation of bluff body turbulent flows using hybrid RANS/LES turbulence models

Ricardo Franco, Cesar Celis[1]

Mechanical Engineering Section, Pontificia Universidad Católica del Perú
Av. Universitaria 1801, San Miguel, Lima 32, Lima, Peru

Luís Fernando Figueira da Silva

Department of Mechanical Engineering, Pontifícia Universidade Católica do Rio de Janeiro
Rua Marquês de São Vicente 225, Rio de Janeiro, RJ 22451-900, Brazil

Institut Pprime UPR3346, Centre National de la Recherche Scientifique, 1 avenue Clément Ader, Futuroscope Chasseneuil 8696L, Francel

[1] Corresponding author – Tel.: +51 1 626 2000 / 4870
E-mail address: ccelis@pucp.edu.pe (C. Celis)

Abstract

Many engineering applications involve turbulent flows around bluff bodies. Because of their intrinsically unsteady dynamics, bluff body characteristic flows feature unique turbulence related phenomena, which makes their numerical modeling challenging. Accordingly, accounting for a circular bluff body flow configuration, three different turbulence modeling approaches are investigated in this work, (i) Reynolds-averaged Navier-Stokes (RANS), (ii) large eddy simulation (LES), and (iii) hybrid RANS/LES. Regarding the hybrid approaches, two variants of the detached eddy simulation (DES) one, delayed DES (DDES) and improved delayed DES (IDDES), are studied. As RANS model, the k-ωSST is utilized here. This RANS model is also used as the background one for both DDES and IDDES. Wall-adaptive local eddy viscosity (WALE) is used in turn as the sub-grid scale (SGS) model for LES. The velocity two-point correlation function is used to assess the mesh size requirements. When compared to experimental data, the obtained numerical results indicate that RANS overestimates the recirculating bubble length by over 18% and is not capable of describing the turbulent kinetic energy and the flow anisotropy in agreement with the experimental data. In contrast, LES, DDES, and IDDES are all within 1% of the recirculating bubble length while predicting both the Reynolds stress tensor components and the corresponding flow anisotropy in agreement with the measurements. Besides, normalized anisotropy tensor invariants maxima in the shear layer were reproduced by all scale resolving models studied here, but they failed to yield the local extrema measured within the wake recirculation region. A comparative analysis of the anisotropic Reynolds stress tensor invariances underscores the adequacy of the scale resolving models.

Keywords: Bluff body, Turbulence modeling, Reynolds-averaged Navier-Stokes, Large eddy simulation, Detached eddy simulation.

Nomenclature

Variables

a_1	Model constant
a_{ij}	Reynolds stress anisotropy tensor
b_{ij}	Normalized stress anisotropy tensor
B_{uu}	Two-point correlation function
$\widehat{B_{uu}}$	Two-point correlation function estimator
C_{d1}, C_{d2}	Model parameters
C_{DES}	Model parameter
C_{μ}	Model parameter
d	Length scale
$\tilde{d}$	DES length scale
d_w	Distance to the nearest wall
d_{LES}	LES length scale
d_{RANS}	RANS length scale
D_b	Bluff body diameter
f_b	Model variable
f_d	Delay function
$\widetilde{f_d}$	Empiric blending function
f_{dt}	Empiric shielding function
f_{μ}	Damping function
F_1	Blending function
F_2	Blending function
h_{max}	Maximum edge length of cell
$-II$	Normalized anisotropy tensor second invariant
III	Normalized anisotropy tensor third invariant
k	Turbulent kinetic energy
k_{∞}	Free stream turbulent kinetic energy
p	Pressure
p_r	Mean relative static gauge pressure
$p_{r_{atm}}$	Atmospheric mean relative static gauge pressure
P_k	Production term

$\tilde{P}_k$	Limited production term
u_j	Velocity vector component
$\bar{u}_j$	Mean velocity vector component
u/U_∞	Mean streamwise velocity
U_∞	Free stream velocity
r_d	Model parameter
r_{dt}	Model parameter
r/D_b	Radial position
r^*/D_b	Non-dimensional radial spatial shift
R_{ij}/U_∞^2	Reynolds stress component
s_{ij}	Non-dimensional strain rate
S	Strain rate
t	Time
x^*	Spatial shift
x_j	Position vector component
x/D_b	Axial position
y^*	Model parameter

Greek-letter variables

α	Model parameter
β^*	Model parameter
β	Model parameters
δ_{ij}	Kronecker delta
Δ	Filter size
ε	Dissipation rate
κ	Von Kármán constant
μ	Molecular viscosity
ν	Kinematic viscosity
ν_t	Eddy viscosity
ρ	Density
σ_k	Model parameter
σ_{w2}	Model parameter
σ_ω	Model parameter
τ_{ij}	Viscous stress tensor
ω	Specific dissipation rate

ω_{ij}	Non-dimensional vorticity tensor

Abbreviations

CFD	Computational fluid dynamics
DDES	Delayed detached eddy simulation
DES	Detached eddy simulation
DFSEM	Divergence-free synthetic eddy method
FSMSP	Freely standing mean stagnation point
IDDES	Improved delayed detached eddy simulation
LES	Large eddy simulation
MSD	Modeled stress depletion
RANS	Reynolds-averaged Navier-Stokes
SGS	Sub grid scale
SST	Shear stress transport
TKE	Turbulent kinetic energy
WALE	Wall-adaptive local eddy viscosity

1 Introduction

Bluff body turbulent flows are present in many engineering applications [1, 2]. For instance, they can be observed when water flows around a submarine, when air flows over a truck or an aircraft, or when wind blows over a building or a bridge. Bluff body flows are also employed in both gas turbine combustors and industrial burners as a means of flame stabilization. The characteristic recirculating flow region formed in this reactive flow related applications has an important effect not only on heat release and flame length [3] but also on pollutant formation. Previous studies have shown that both the turbulence intensity levels [4] and the size of the recirculating bubble [5] exert an effect on NO_x emissions. Regarding soot, it has been found that increasing turbulence intensity leads to a decrease in soot formation [6]. In these applications, therefore, the turbulent characteristics of the associated bluff body flows have a direct effect on the production of pollutants. More specifically, the interaction between the time and length scales characterizing turbulent reacting flows controls the pollutant formation in flames. It is worth recalling as well that the flame behavior may be very sensitive to boundary conditions [7, 8]. As a consequence, experimental studies aiming to define and validate a computational problem should document then these conditions as thoroughly as possible [7]. Due to the associated complexities, specifically, an adequate characterization of the turbulent flow present in bluff body like configurations must then be performed before improving existing combustion models.

In general, there are two turbulence modelling approaches that can be used in numerical simulations of practical interest devices, i.e., Reynolds-averaged Navier-Stokes (RANS) and large eddy simulation (LES). RANS modelling consists of solving time- or ensemble-averaged equations, whereas LES involves solving filtered equations [9]. Over the years, to deal with the associated turbulent closure problem arising when using these two modelling approaches, different turbulence models have been developed. Typical two-equation RANS models, based on a linear stress-strain relationship assuming isotropic turbulence, fail to properly describe separated flows due to their expected anisotropy [5, 10]. Thus, nonlinear models have been developed in order to improve upon such linear models [9]. Nevertheless, recent works on turbulent flows characterizing bluff body like configurations showed that, even if nonlinear models improve the predictions

performed, they still do not reproduce the measured results [11]. Notice that the anisotropic turbulence component is the main responsible for the turbulent transport of momentum [9]. It is important, therefore, that anisotropy be properly captured by numerical models, especially in reacting flows. As highlighted above, since combustion is highly sensitive to the local turbulent state, the accurate modelling of turbulence is paramount to obtaining reliable turbulent combustion results.

For bluff body turbulent flows, LES has been shown to produce more than acceptable results in the past [5, 10, 12]. Because of the much higher computational cost involved, however, LES has yet to meet a widespread use in industry. In near wall regions, for instance, a very high resolution is required to yield accurate results. To overcome this near wall challenge, detached-eddy simulation (DES) has been developed as an alternative modelling approach. Indeed, DES combines both RANS and LES techniques, switching between both depending on grid density and turbulent length scales [13]. This enables relaxing to RANS solutions at near wall regions with relatively coarse meshes, and to LES ones over larger eddies in the farther regions. One of the major DES disadvantages relates to its sensitivity to sudden grid refinement near boundary layers. Indeed, a process called modeled stress depletion (MSD) is known to arise in regions of ambiguous grid spacing or sudden grid refinement, near wall boundaries, for example, where the switch from RANS to LES significantly reduces the eddy viscosity due to weak flow instabilities [14, 15]. Ambiguous grid spacing occurs when cells are small enough to trigger a switch to LES but not small enough to support accurate solutions [16]. Notice that the main problem caused by MSD is usually grid induced flow separation. Other DES variants, such as the delayed DES (DDES), and the DDES with improved wall modeling (IDDES), have been thus developed in an attempt to avoid this shortcoming [15–17]. Both DDES and IDDES, which intend to remain in RANS mode in near-wall and boundary layer regions, hence avoiding MSD, are studied here.

Accordingly, in this work, the turbulent near wake flow behavior of a circular bluff body configuration is numerically studied using the open source computational fluid dynamics (CFD) tool OpenFOAM v2006 [18]. Both time-averaging and scale resolving modeling techniques are employed. Regarding the scale resolving techniques employed here, a standard LES with a wall-adaptive local eddy viscosity (WALE) [19] sub-grid scale model are compared to DDES and IDDES, both using *k-ω SST* as the approach for the background model [15]. The k-ωSST [14] is also used as a standalone RANS model.

The obtained numerical results are compared with existing turbulence experimental data [20], in terms of mean velocity fields and turbulent variables such as turbulent kinetic energy (TKE), Reynolds stress anisotropy and anisotropy invariants. The main goal here is to assess the predicting capabilities of hybrid RANS/LES approaches to properly predict bluff body turbulent flows as those studied here. More specifically, the expectation is that IDDES improves upon DDES as it has additional improvements and corrections that should produce results that are more accurate. Specifically, accounting for the associated computational costs as a limiting factor, it is of particular interest here to analyze the level of mesh refinement required to yield accurate results using these hybrid approaches. The motivation for this comes from the fact that this turbulence modeling framework will be used in future to predict soot formation in turbulent reacting flows, including detailed soot formation models and chemical kinetic mechanisms featuring thousands of chemical reactions and hundreds of chemical species [21].

Similar bluff body turbulent flows studies [5] developed in the past involved both inert and reactive analyses, where mean flow variables and second order moments were compared and validated against experimental data. LES has also been used to characterize a bluff body configuration using OpenFOAM at two Reynolds numbers [10, 22], where different flow features, vorticity fields, and pressure coefficients were analyzed. To the best of the authors' knowledge, however, no previous work performed anisotropic turbulence invariants analyses as those carried out here. Notice that anisotropic stress invariants are concise and synthetic indicators of turbulent anisotropy, independent from the coordinate system. Additional contributions of this work relate to the performance assessment of different DES alternatives in comparison to more proven LES techniques. Accordingly, Sections 2 and 3 respectively describe the mathematical and numerical modeling employed here. In Section 4, the main results are presented and discussed, in both qualitative and quantitative terms. Finally, Section 5 summarizes the main conclusions drawn from the results obtained here.

2 Mathematical Model

The mathematical model used in this work is briefly described in this section.

2.1 Governing Equations

Mass and momentum transport equations [9] have been solved in this work. The air flow is treated as incompressible here because of the relatively low flow Mach number (≈0.03) accounted for. Furthermore, it has been shown that using a compressible setup for a low Mach bluff body flow introduces inaccuracies in the form of spurious oscillations in high grid density regions [10]. Accordingly, the solved equations read as,

$$\frac{\partial u_j}{\partial x_j} = 0, \tag{1}$$

$$\frac{\partial u_j u_i}{\partial x_j} = -\frac{\partial p}{\partial x_i} + \frac{\partial \tau_{ji}}{\partial x_j}, \qquad i = 1,2,3. \tag{2}$$

Eqs. (1) and (2) describe the temporal (t) and spatial (x_i) variations of both pressure p and instantaneous velocity u_i. Notice that the viscous stress tensor (τ_{ij}) is determined using a Newtonian fluid hypothesis,

$$\tau_{ij} = \nu\left(\frac{\partial u_i}{\partial x_j} + \frac{\partial u_j}{\partial x_i}\right), \tag{3}$$

where ν is the kinematic viscosity and δ_{ij} the Kronecker delta. Depending on the modeling approach (RANS or LES) used in this work, Eqs. (1) and (2) are either ensemble-averaged or spatially filtered [9] at a posterior step.

2.2 Turbulence Modeling

The flow governing transport equations are seldom solved directly, especially in turbulent flows. This is because the computational cost involved when solving all time and length scales present in high Reynolds number flows is prohibitively expensive. The large range of turbulence scales requiring for their solution both extremely high grid resolution and small time steps are the main responsible for these computational costs [23]. Therefore, modelling techniques are usually applied for solving turbulent flows. Two general approaches used in practical situations to model turbulence, RANS and LES, are briefly described here. Hybrid approaches such as DES, which combines both RANS and LES, are often a practical choice as well, and are also addressed in this section.

2.2.1 RANS approach

In RANS-based approaches, to solve for mean flow quantities, the Navier-Stokes equations [Eqs. (1) and (2)] are time- or ensemble-averaged depending on the type of simulations accounted for, steady or unsteady. When carrying this averaging, however, an extra term needing closure arises. This term, known as Reynolds stress, needs to be modeled to provide closure to the equations. In the present work, the $k\omega SST$ model is used for the referred closure. Two additional equations are introduced by this model [14],

$$\frac{\partial k}{\partial t} + \frac{\partial \bar{u}_j k}{\partial x_j} = \tilde{P}_k - \frac{k^{1.5}}{d_{RANS}} + \frac{\partial}{\partial x_i}\left[(\nu + \sigma_k \nu_t)\frac{\partial k}{\partial x_i}\right], \tag{4}$$

$$\begin{aligned}\frac{\partial \omega}{\partial t} + \frac{\partial \bar{u}_j \omega}{\partial x_j} = \alpha S^2 - \beta \omega^2 + \frac{\partial}{\partial x_i}\left[(\nu + \sigma_\omega \nu_t)\frac{\partial \omega}{\partial x_i}\right] \\ + 2(1 - F_1)\sigma_{w2}\frac{1}{\omega}\frac{\partial k}{\partial x_i}\frac{\partial \omega}{\partial x_i}, \qquad i,j = 1,2,3\end{aligned} \tag{5}$$

where,

$$\tilde{P}_k = \ min(P_k, 10 \cdot \beta^* k\omega), \tag{6}$$

$$P_k = \nu_t \frac{\partial \bar{u}_i}{\partial x_j}\left(\frac{\partial \bar{u}_i}{\partial x_j} + \frac{\partial \bar{u}_j}{\partial x_i}\right), \qquad i,j = 1,2,3 \tag{7}$$

$$\nu_t = \frac{a_1 k}{max(a_1 \omega, SF_2)}. \tag{8}$$

Notice that a RANS-related length scale $d_{RANS} = k^{0.5}/(\beta^* \omega)$ has been included in Eq. (4) to account for the fact that hybrid DDES and IDDES models will modify its behavior. This model is computationally inexpensive and will serve as a baseline for more complex scale resolving approaches. For further information regarding this model, such as the definition of the blending functions F_1 and F_2, the reader is encouraged to review reference [14].

2.2.2 LES and DES approaches

LES equations are obtained after spatially filtering the Navier-Stokes ones, Eqs. (1) and (2). The filter size (Δ) is defined here by the grid resolution. The open sub-grid scale (SGS) related terms resulting from the filtering processes are modeled to provide closure. Classically, it is assumed that the smaller turbulent scales tend to be isotropic, so they are more accurately modeled using isotropic assumptions [9]. This results in only a percentage of the TKE to be resolved and the remaining part is modeled. Typically, at least 80% of the TKE needs to be resolved for an LES simulation to be considered accurate [24]. In this work, a standard LES with a WALE [25] sub-grid scale model is utilized. Despite the markedly improved accuracy upon RANS, and due to the associated increased computational cost, LES has not seen yet a widespread industrial use. DES, a hybrid RANS/LES approach dynamically switching between RANS and LES depending on the grid size and the length scale (d), represents thus an alternative approach. The length scale $\tilde{d}$ defining the RANS or LES mode of the model in this case is computed from an expression of the form [15, 25],

$$\tilde{d} = min(d_{RANS}, d_{LES}), \tag{9}$$

$$d_{LES} = C_{DES} h_{max}, \tag{10}$$

where h_{max} represents the maximum edge length of the computational grid cell and C_{DES} is a model constant equal to 0.82. Notice as well that d_{LES} refers to the reference length scale for LES mode utilized by hybrid models such as DDES and IDDES.

As highlighted in Section 1, in regions of ambiguous grid density, MSD can occur leading to numerically induced flow separation. DDES modeling, a DES variant, accounts for both the distance to a wall and the eddy viscosity. The model can then detect if a boundary layer is present, prolonging thus the full RANS mode [16]. The model utilized as the background model in RANS mode is used as the SGS model in LES mode. For both DES and DDES, the length scale for the RANS model is defined as $d_{RANS} = k^{0.5}/(\beta^* \omega)$, where $\beta^* = 0.09$ [13]. DDES includes a delay function f_d that modifies this length scale d_{RANS} and defines a new length scale $\tilde{d}$ as follows [17],

$$f_d = 1 - tanh[(C_{d1} r_d)^{C_{d2}}], \tag{11}$$

$$r_d = \frac{\nu_t + \nu}{\kappa^2 d_w^2 [0.5(S^2 + \Omega^2)]^{0.5}}, \tag{12}$$

$$\tilde{d} = d_{RANS} - f_d max(0, d_{RANS} - d_{LES}), \tag{13}$$

where S and Ω represent, respectively, the magnitude of the strain rate and vorticity tensors, $C_{d1} = 20$, $C_{d2} = 3$, κ is the von Kármán constant, and d_w is the distance to the nearest wall [15]. Notice that when $f_d = 1$, then $\tilde{d} = min(d_{RANS}, d_{LES})$. Conversely, when $f_d = 0$, then $\tilde{d} = d_{RANS}$, which means that the model is forced to run in RANS mode in spite of the grid characteristics [17]. For further details about these models, the interested reader is encouraged to refer to references [13–17, 25].

Over the years, additional modifications have been made to the DES model to produce the improved delayed DES (IDDES) one. This last model modifies the length scale definition according to [15],

$$\tilde{d} = \widetilde{f_d} \cdot d_{RANS} + \left(1 - \widetilde{f_d}\right) \cdot d_{LES}, \tag{14}$$

$$\widetilde{f_d} = max[(1 - f_{dt}), f_b], \tag{15}$$

$$f_{dt} = 1 - tanh[(C_{dt1} \cdot r_{dt})^{C_{dt2}}], \tag{16}$$

$$r_{dt} = \frac{\nu_t}{\kappa^2 d_w^2 [0.5(S^2 + \Omega^2)]^{0.5}}, \tag{17}$$

$$f_b = min[2\, exp(-9\alpha^2)\,, 1.0], \tag{18}$$

$$\alpha = 0.25 - \frac{d_w}{h_{max}}, \tag{19}$$

where $C_{dt1} = 20$ and $C_{dt2} = 3$. Notice that in this work, in accordance with the findings of [15], the model coefficients are set to OpenFOAM's default values. In addition to avoiding MSD and grid induced separation, the IDDES formulation also aims at resolving log-layer mismatches in wall-bounded layers [16].

In the present work, the WALE sub-grid scale model is evaluated, along with the DDES and IDDES approaches. Following [15], both DDES and IDDES use here k-ω SST [14] as the background model.

3 Numerical Model

The numerical model used in this work is described in this section. An emphasis is put on the solver and numerical schemes, the geometric configuration, the spatial and temporal discretizations utilized, and the boundary conditions imposed.

3.1 Solver and Numerical Schemes

The standard *pisoFoam* solver based on the PISO algorithm [26] available in OpenFOAM v2006 [18] has been used in this work. The governing equations temporal derivatives are discretized by a second order backward-differencing scheme. The corresponding gradients are in turn discretized using a second order centered-difference scheme as well as for the divergence terms. Finally, the Laplacian terms are discretized by a corrected linear scheme. The discretization schemes utilized guarantee that the solution is second-order accurate [27].

3.2 Geometric Configuration

Both the bluff body geometric configuration accounted for and the associated computational domain numerically simulated here (Fig. 1) have been configured according to the experimental setup [20] providing the data used as reference here. As noticed in Fig. 1 left plot, a 200 mm long annular duct has been simulated to minimize numerical diffusion of the inlet boundary conditions. In addition, outlets have been placed far enough away to avoid affecting the region of interest, which is the bluff body near wake. Domain independence studies have been initially carried out by extending the domain length more than four times its current value, proving that its current size does not affect the flow field in the referred region of interest. Fig. 1 left plot illustrates, in particular, the bluff body diameter ($D_b = 60$ mm) and the main geometric parameters accounted for.

3.3 Mesh Generation

An O-grid type structured mesh (Fig. 1 right plot) has been generated using *blockMesh* and refined in a sequence of stages of *refineMesh* to concentrate the

computational resources in the critical regions near the separation point and the free shear layer. Both tools are provided by OpenFOAM. Notice the darker (denser) regions in the near-wake region and particularly in the region close to the expected flow separation points. The final computational meshes used here feature about 6 million cells. Most of these mesh elements are concentrated near the wall and in regions close to the wake. The smallest cells have a streamwise length of approximately 0.2 mm and a radial length of approximately 0.1 mm. Far from the region of interest, the biggest computational cells have a maximum size of 10 mm to keep computational resources focused on the critical zones. Geometric growth rates within the region of interest are minimal, cells are progressively refined until the cells have apparent hanging nodes. However, OpenFOAM treats these as polyhedral cells rather than hanging nodes. Outside the region of interest, the growth rate is set at 15% until the 10 mm limit is reached.

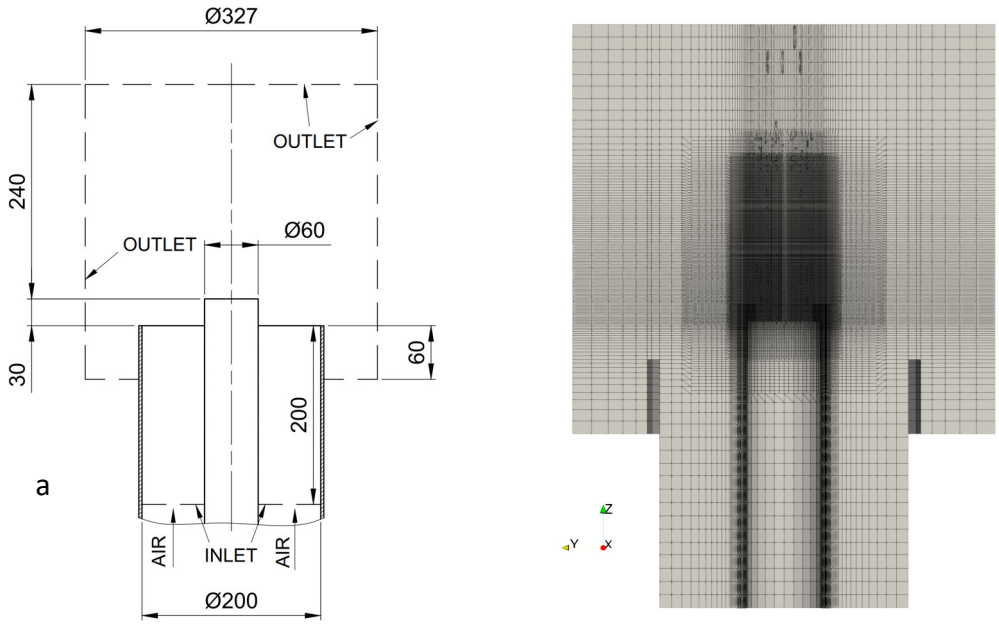

Fig. 1 Geometric configuration and computational domain (*a*), dimensions in mm. Computational mesh 3D cross-section (*b*).

It is worth noticing here that the referred computational meshes has been chosen after carrying out mesh quality analyses based on two-point correlations. For an arbitrary velocity component u in an arbitrary direction x, the two-point correlation function is defined as,

$$B_{uu}(x^*) = \frac{E_x[u'(x)u'(x-x^*)]}{E_x[u'(x)^2]}, \tag{20}$$

where u' represents the fluctuation of u and $E_x[\cdot]$ the expected value evaluated in the x direction [28]. Notice that an expected value is a probabilistic concept, and in this case it implies an integration along the arbitrary direction x. Thus, the two-point correlation function must be estimated statistically, involving a summation over a series of sampled x_i values. Also, any estimate requires an estimator, which generally may be deduced by leveraging the law of large numbers. By replacing each expected value in Eq. (20) by its corresponding sample average summing over the aforementioned series of x_i values, the estimator $\widehat{B_{uu}}(x^*)$ of $B_{uu}(x^*)$ is written as,

$$\widehat{B_{uu}}(x^*) = \frac{{}^1\!/_n \sum_i u'(x_i)u'(x_i-x^*)}{{}^1\!/_n \sum_i u'(x_i)^2}. \tag{21}$$

Notice that the estimate consists of the quotient of two separate sample averages. The law of large numbers requires a sufficiently large sample size for the estimates to be accurate. Given that a function is being estimated, estimates must be computed for different values of x^* and each of them must satisfy the law of large numbers' requirements.

Three different mesh resolutions (2.6M, 4.4M and 6M cells) have been evaluated in this using the WALE model and their corresponding results are shown in Fig. 2. When the correlation between two points is lower than 0.3 in absolute value it is said that the fluctuations are no longer correlated and do not belong to the same turbulent structure [28, 29], hence the reference dotted red line drawn at this value. The sample size for each mesh assessed here consists of 896 radial segments, extracted as subsamples of 128 lines distributed uniformly around the bluff body symmetry axis at 7 different time snapshots, spaced every 0.1s. Before averaging them, the fluctuations are transformed to cylindrical coordinates. Notice that the axial component B_{uu} shows a slightly higher sensitivity to mesh size changes compared to the radial (B_{vv}) and azimuthal (B_{ww}) components. The difference in the referred sensitivity may be inferred by the changes in the curves when increasing resolution, particularly the increase in average length scale displayed in the 4.4M results compared to the 2.6M results. Typically, average length scale should decrease when increasing resolution due to the smaller scales being resolved. Moreover, this increase in average length scale may indicate that larger sample sizes would yield improved estimates. From Fig. 2 results, based on the progressive convergence and

similarity of the two-point correlation function curves, particularly B_{vv} and B_{ww}, the computational mesh featuring about 6M elements is chosen due to its greater resolution while remaining computationally feasible when compared to the other two coarser meshes considered.

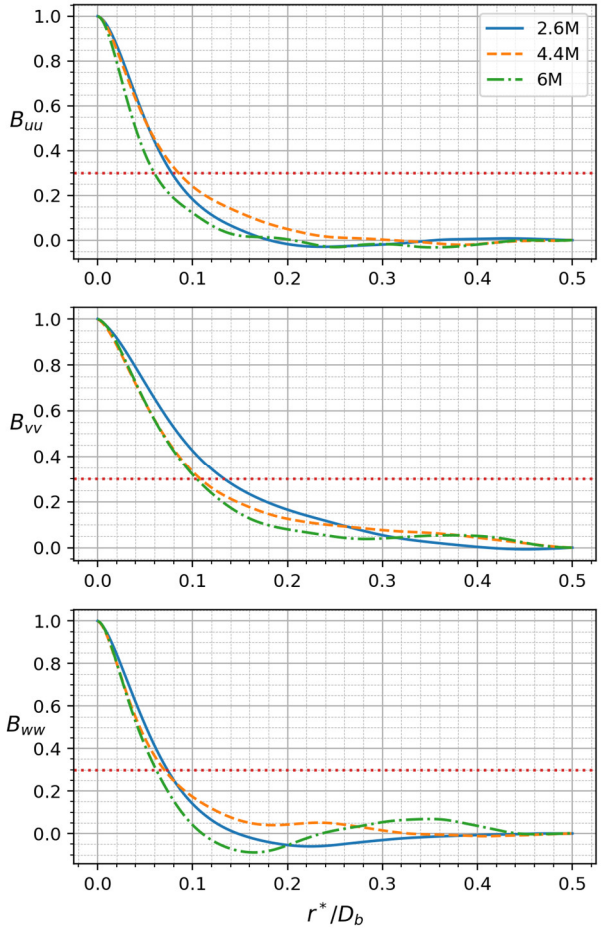

Fig. 2 Two-point correlation functions of three velocity components evaluated from $r/D_b = 0$, $x/D_b = 0.5$ to $r/D_b = 0.5$, $x/D_b = 0.5$ in the radial direction. r^*/D_b refers to the spatial shift at which the two-point correlation is evaluated.

The influence of the model on the two-point correlation has not been analyzed. Future studies could focus on the effects of the background models in hybrid approaches on these quantities. Perhaps the added viscosity present in DES models influence the vortices present in the recirculation zone.

3.4 Boundary and Initial Conditions

In the LES and DES-based simulations carried out here, a divergence-free synthetic eddy method (DFSEM) [30] was used at the inlet boundary to reproduce the turbulent flow measured in the corresponding experiments [20]. Preliminary numerical trials were performed using, first a uniform constant velocity field and, later, adding a white noise generator to model turbulence. These attempts performed poorly, since neither the freestream nor the near wake flow agreed with the experimental data. To obtain an inlet free stream in agreement with the measurements, which are characterized by a mean velocity of $U_\infty = 11.8\, m/s$ and a mean TKE of $k_\infty = 1.4\, m^2/s^2$ [20], a parametric study involving the main settings of the DFSEM synthetic turbulence generator was then carried out. The parameters which produced an inlet flow most similar to the experimental one were an average length scale of 6 mm, an average velocity of $11.5\, m/s$, and a uniform, axisymmetric anisotropic Reynolds stress tensor featuring a radial component of $20\, m^2/s^2$, an axial component of $8\, m^2/s^2$, and an azimuthal component of $20\, m^2/s^2$. At the inlet, $\partial p/\partial n = 0$. At the domain outlets, pressure was set at a fixed value, whereas $\partial u_i/\partial n = 0$. The computational domain was initialized with a converged RANS simulation to reduce computational time spent on transient flow state.

Hereinafter, all dimensions, velocities and turbulent variables referred throughout this work are non-dimensionalized by D_b, U_∞ and U_∞^2 respectively. All spatial derivatives are non-dimensionalized, in turn, by D_b/U_∞.

4 Results and Discussion

In this section, the main numerical results obtained in this work will be presented and contrasted with measurements available [20]. First, classical mean flow variables will be discussed. Next, second order moments will be particularly analyzed both qualitatively and quantitatively. Finally, the anisotropy tensor invariants behavior will be examined. Overall, the numerical predictions carried out by the scale resolving turbulence models used here will be seen to approximate more closely the experimental measurements, whereas the time-averaging one to deviate the furthest. For the sake of brevity hereinafter, WALE will refer to the results computed by the WALE SGS model and RANS to the *k*-

ωSST results. Since both hybrid RANS/LES models employed in this work use the same background model, *k-ωSST,* they will be referred to as DDES and IDDES.

4.1 Flow velocity field

A first comparison between computed and measured results employs the classical representation of the evolution of the streamwise velocity u/U_∞ along the bluff body centerline, Fig. 3. The recirculating flow zone length and the minimum u/U_∞ values are further emphasized in Table 1. Regarding the flow recirculation zone, the IDDES result is the closest one to the experimental data overestimating it by 0.1%, however its performance in capturing the velocity profile before the stagnation point is clearly worse when compared to both WALE and DDES. In turn, WALE underestimates it by 0.6% and DDES overestimates it by 1.0%. Notice that the typical reported experimental uncertainty is 3.6% [20], which indicates that all scale resolving models reproduce the average flow behavior within this uncertainty. In contrast to these results, the recirculation zone length predicted by RANS is overestimated by about 18%. Even though the RANS model fails to describe this crude flow structure measure associated to the recirculation zone length, further comparisons will also include this model so that a thorough discussion of each model prediction capability may ensue.

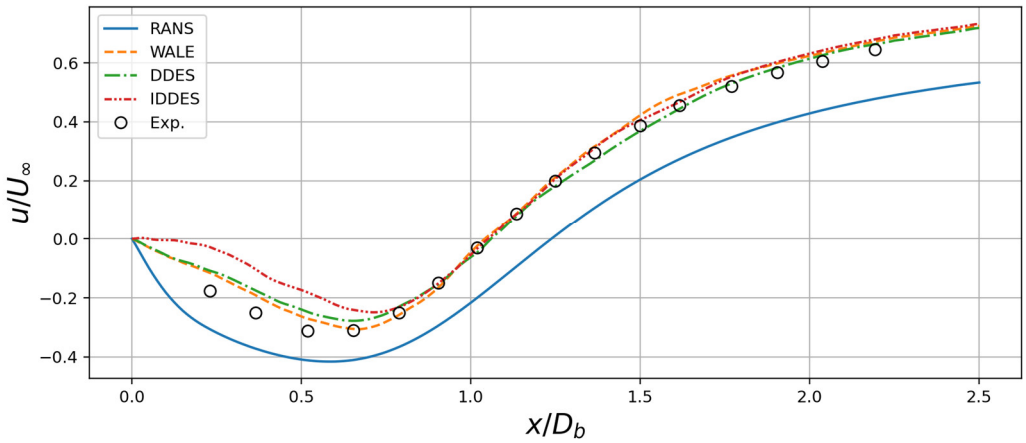

Fig. 3 Evolution of the mean streamwise velocity u/U_∞ along the bluff body centerline of RANS, WALE, DDES and IDDES models compared to the experiment.

Table 1 RANS, WALE, DDES and IDDES predictions of both recirculation zone length normalized by D_b and minimum u/U_∞ in the centerline with their corresponding percentual deviations from the experiment.

	Experiment	RANS	WALE	DDES	IDDES
Recirculation Length [-]	1.048	1.240	1.041	1.059	1.050
Deviation [%]	-	+18%	-0.6%	+1.0%	+0.1%
Minimum u/U_∞ [-]	-0.318	-0.416	-0.306	-0.278	-0.249
Deviation [%]	-	-31%	+3.8%	+13%	+22%

Notice that the recirculating flow zone length is the distance from the bluff body's top face to the freely standing mean stagnation point (FSMSP). In this case, due to the coordinate system employed, the numerical value of the axial coordinate of the FSMSP coincides with the recirculating zone length. In 4, the u/U_∞ fields for all turbulence models studied here are depicted. Notice that every model predicted the toroidal vortex coherent structure observed in the experimental near wake, albeit with some minor differences in most cases. A notable feature revealed by the average streamlines is the presence of the aforementioned FSMSP, which will be used herein as a singular reference position in the flow field. The streamlines that originate at the vicinity of the bluff body rim converge to the FSMSP neighborhood. By following such streamlines, it may be observed both a flow structure initially resembling that of a shear layer, and a strong streamline curvature at the vicinity of the referred stagnation point indicating the presence of flow rotation. Even if all turbulence models studied here qualitatively reproduce the overall flow structure, only the scale resolving ones seem to adequately describe this shear layer spread and the recirculation zone dimensions. Indeed, the RANS model clearly leads to an unduly elongated recirculation zone. These qualitative characteristics will be shown to be related to the turbulence anisotropy present in the flow (Section 4.5).

To further clarify the expected structure and location of the aforementioned flow features such as the FSMSP and shear layer and wake regions, the interested reader is encouraged to refer to the experimental work used for comparison purposes here by Cruz et al. [20]. Notice from the referred work (Fig. 2 specifically), the FSMSP position at the centerline, the shear layer region located between the $u = 0$ line and the wake region limit, and the wake region itself downstream the stagnation point.

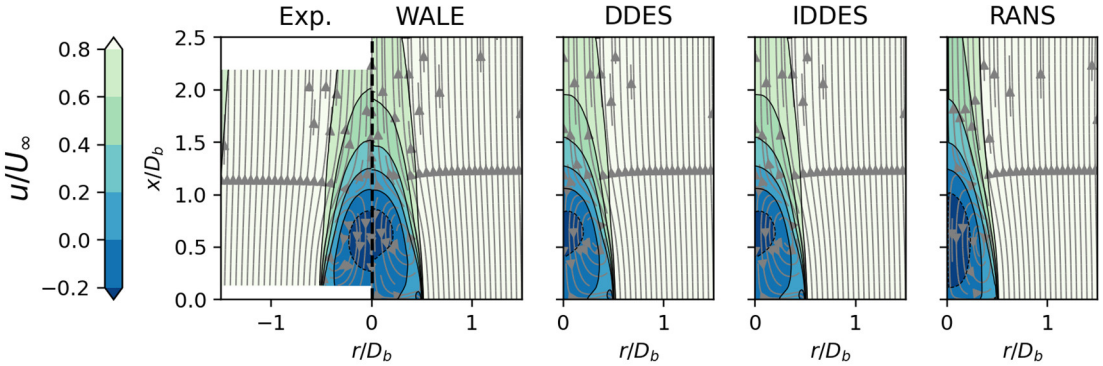

Fig. 4 Mean streamwise velocity $\boldsymbol{u/U_\infty}$ contours and streamlines of the experimental, RANS, WALE, DDES and IDDES results.

In order to quantitatively compare numerical and experimental results, Fig. 5 gives the radial profiles of the axial velocity component at different streamwise positions. The agreement may be seen to lie within the experimental uncertainty range, which is of 3.6 % in low shear regions [20]. In particular, WALE and DDES were found to be able to predict both the velocity deficit within the recirculation zone and the velocity gradient between this zone and the freestream flow. However, IDDES struggled to describe the recirculating velocity at $x/D_b = 0.2$, $r/D_b < 0.5$. Nevertheless, the RANS results do exhibit some discrepancies, particularly, with respect to the boundary layer behavior at the upstream position, $x/D_b = 0.2$, i.e., at the vicinity of the bluff-body rim. The origins of such these discrepancies are now examined.

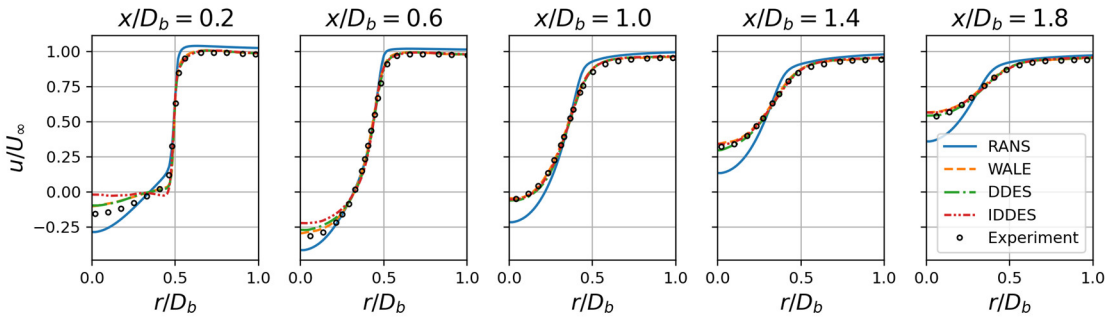

Fig. 5 Mean streamwise velocity $\boldsymbol{u/U_\infty}$ radial profiles at five different axial positions. Experiments: symbols. Computations: lines. $\boldsymbol{x/D_b}$ is the non-dimensional axial distance.

4.2 Boundary layer thickness

First, it is worth paying attention to the small secondary vortex predicted numerically near the bluff body rim ($x/D_b = 0$, $r/D_b = \pm 0.5$), which is more easily noticed in Fig.

6. Due to the experimental constraints regarding the range of x/D_b values where is feasible to carry out measurements, this flow feature was not captured in the experimental work [20] used for comparison purposes here. Accordingly, the mean flow structure quantitative discrepancies apparent in Fig. 4 may also be partially associated with the resolved boundary layer or lack thereof. In this context, it is important to observe the $x/D_b = 0.2$ streamwise velocity profiles close to $r/D_b = 0.55$ shown in Fig. 5. While all scale resolving turbulence models display a slight velocity increase at the bluff body vicinity, in contrast to the experimental measurements, RANS exacerbates this behavior the most. From Fig. 5 is also noticed that the RANS free stream velocity is higher than that predicted by the other models. It seems that this outcome is related to the flat velocity profile applied at the inlet boundary conditions. As the flow near the walls is slowed down due to the no slip condition, the free stream velocity should accelerate slightly to preserve mass continuity. A closer view into the matter at hand is provided in 6. Since the boundary layer thickness may be estimated by the distance between the $u/U_\infty = 0.99$ surface and the bluff body rim near the separation point ($x/D_b = 0, r/D_b = 0.5$), when compared to RANS, the three scale resolving models, i.e., WALE, DDES and IDDES, seem to describe a significantly thicker boundary layer. As a consequence, the secondary vortex in the RANS case is almost nonexistent. Besides, the hybrid RANS/LES models predict boundary layers slightly thicker than the one predicted by WALE. Notice that the WALE boundary layer has a nondimensional boundary layer thickness of 0.11 while for both hybrid models show a thickness around 0.13. As highlighted in Section 1, this is an expected outcome because, when compared to hybrid models, LES modelling requires higher near-wall resolutions for the computation of boundary layer developments. Since the flow recirculation region studied here is originated from the flow separation at the bluff body rim, the flow directed towards the FSMSP is expected to be influenced by the referred boundary layers and their properties (thicknesses). For instance, the higher flow velocities present in the RANS wake could be explained by the increased momentum at the boundary layer developing along the bluff body surface aligned with the streamwise direction.

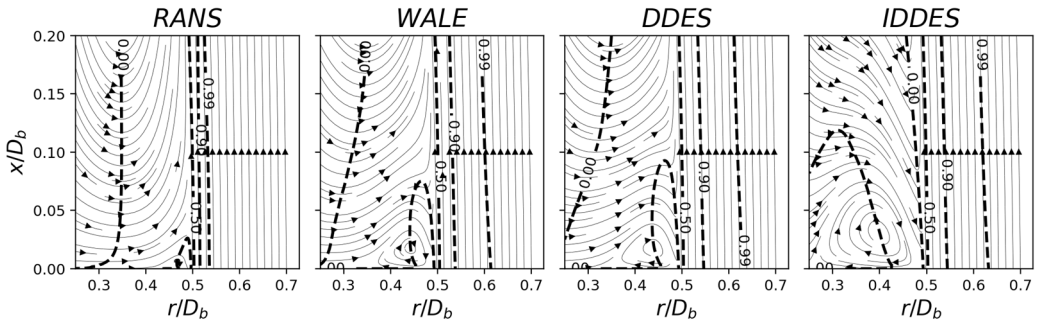

Fig. 6 Mean streamwise velocity contour lines and depiction of secondary vortices formed at the vicinity of the bluff body rim. $\boldsymbol{u}/\boldsymbol{U}_\infty$ isocurves correspond to the labeled values.

As underscored by the flow streamlines shown in Fig. 4, momentum from the near-wall region is transported to both the wake downstream the FSMSP and the recirculating flow region. Therefore, higher velocities associated with the RANS computed boundary layer seem to introduce as well increased angular momentum to the vortex. It could be inferred therefore that slower boundary layer velocities would lead to reduced recirculating and wake flow velocities. This would explain why the scale resolving models predict flow wakes that are more similar to the experiment one than RANS. It must be recalled here that the hybrid models are able to alternate depending on grid resolution between time-averaging and scale resolving approaches, enabling thus improved near-wall descriptions. Although the scale resolving models improve upon RANS regarding the formation of the aforementioned boundary layer, some discrepancies still remain. This aspect can be particularly observed at $x/D_b = 0.2$ and at $x/D_b = 0.6$. At these two axial positions, Fig. 5 shows that WALE and DDES predict similar velocity profiles, but the one predicted by IDDES is slightly worse at $x/D_b = 0.6$. However, at $x/D_b = 0.2$, IDDES fails to predict the streamwise velocity profile within the recirculation zone ($r/D_b < 0.5$). Notice the contrast between the LES/DDES streamlines with the ones produced by IDDES shown in Fig. 6. While the former are in qualitative agreement, the latter appears to be influenced by the significantly larger secondary vortex, as the streamlines do not curve as smoothly towards the free stream, rather they sharply turn when influenced by the shear layer. As it will be further analyzed in Section 4.4, the discussed boundary layer behavior also affects the wake turbulence levels.

4.3 Pressure field

Pressure-related measurements are not available in the set of experimental data used as reference. Even so, an insight about the overall flow structure could be gathered by examining the computed mean relative static gauge pressure p_r fields. As shown in Fig. 7, all four turbulence models employed here agree on the qualitative structure of the pressure field. First, notice how all used models agree that the shear layer flows through a slightly favorable pressure gradient from $x/D_b = 0$ up to $x/D_b \approx 0.6$, quickly increasing afterwards and becoming significantly adverse towards the FSMSP. Half a bluff body diameter downstream this point, the pressure decreases towards the far wake and the recirculating flow region. The recirculating flow region is characterized indeed by a pressure minimum. Moreover, all turbulence models coincide that the minimum pressure is found in the vortex center. Except in the RANS case, a similar pressure behavior characterizes the FSMSP downstream region, where the maximum p_r values are located away from the symmetry axis, i.e., at ($x/D_b \approx 1.4$, $r/D_b \approx 0.4$). The gentler gradient and lower p_r maximum computed by RANS could be associated with an excessive turbulence dissipation rate, which assumes isotropy at the smallest turbulent scales.

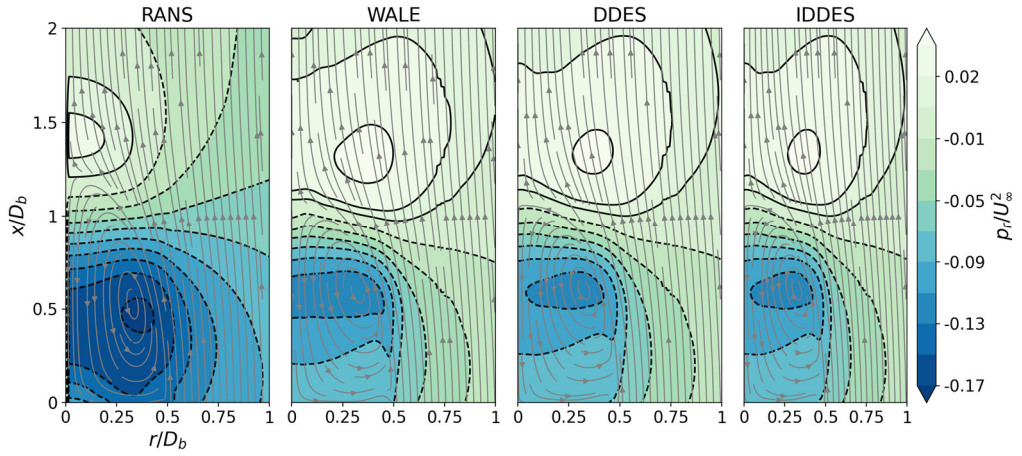

Fig. 7 Mean relative static gauge pressure p_r fields. $p_{r_{atm}} = 0$.

4.4 Turbulent kinetic energy and Reynolds stress tensor

In order to characterize the overall turbulent state within the bluff body near wake, the turbulent kinetic energy (TKE) fields numerically obtained in this work are presented in Fig. 8, along with the corresponding measurements. Regarding the experimental data,

it is worth noticing first that the global maximum TKE value was measured in the vicinity of the FSMSP. Upstream the FSMSP and within the recirculating flow region, TKE decreases. Toward the bluff body, within the recirculation zone, the TKE exhibits a weak decrease along the radial direction. Outside the recirculation zone, TKE features a local maximum along the shear layer separating the recirculating flow region and the free stream. Downstream the FSMSP toward the far end of the wake, the TKE also decreases in the streamwise direction. In contrast with the recirculating flow region, however, downstream the FSMSP, the turbulence monotonically decreases with the radial position. In other words, at any given streamwise position downstream the FSMSP, the maximum TKE lies at the centerline. Although turbulence along the shear layer may be associated with the presence of a significant strain rate, the same cannot be said about turbulence in the vicinity of the FSMSP. Indeed, the dominant mechanisms leading to these turbulence extrema are different, and seem to be related to streamline curvature, which in turn leads to Reynolds stress anisotropy.

As shown in 8, compared to the scale resolving turbulence approaches, the RANS agreement with the considered experimental data in terms of TKE is still lacking. Specifically, the RANS model wrongly predicts that the maximum TKE is located at the shear layer, whereas at the vicinity of the FSMSP a saddle region is formed. In addition, the turbulence intensity is underpredicted by this model. Contrary to the experimental results as well, the RANS predicted TKE in the near wake upstream the FSMSP is weakly dependent on the radial position. It is worth noticing here that the overall turbulence in the bluff body wake promotes the mixture of relatively low momentum fluid present in the recirculation zone with the free stream. When using the scale resolving models, in turn, the maximum TKE is correctly located at the vicinity of the FSMSP, but the turbulent intensity is overestimated. Indeed, when compared to the other two scale resolving models used here, the IDDES overestimates the TKE the most, i.e., up to 40% at $x/D_b = 1.0$. In spite of these discrepancies, the scale resolving models used in this work seem to successfully describe the TKE at the wake. In addition, they correctly predict that the TKE remains independent of the radial coordinate within the recirculation zone, while decreasing from the FSMSP. These models, especially WALE and DDES, also agree with the turbulence being generated at the shear layer before converging towards the FSMSP. Contrarily to what is observed in the RANS predictions, the inverse

proportionality between TKE and the radial position within the wake downstream the FSMSP is well described by the assessed scale resolving turbulence models.

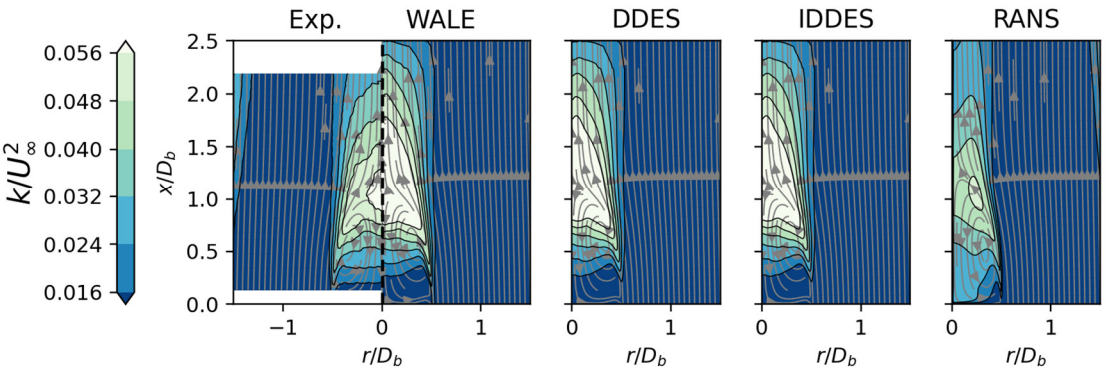

Fig. 8 Turbulent kinetic energy k/U_∞^2 contours and streamlines of the experimental, RANS, WALE, DDES and IDDES results.

Further insight on the turbulent flow predictions may be obtained by examining Fig. 9, which presents in turn the radial profiles of three components of the Reynolds stress tensor. Notice first from this figure that the experimental results present extrema for both the streamwise (R_{xx}/U_∞^2) and radial (R_{rr}/U_∞^2) components at the vicinity of the bluff body rim separation point ($x/D_b = 0.2$, $r/D_b = 0.5$). It is also worth observing that beyond $x/D_b = 0.2$ the position of the maximum R_{xx}/U_∞^2 moves towards the centerline along the shear layer, with $x/D_b = 1.0$ presenting the global maximum. The location of the maximum R_{rr}/U_∞^2 values depart from the shear layer, reaching the centerline as the flow converging at the FSMSP promotes mixing. Even if the discussion on anisotropy is deferred to the following section, in this figure it may be observed first that, at the vicinity of the FSMSP, R_{rr}/U_∞^2 is significantly larger than R_{xx}/U_∞^2. The R_{rr}/U_∞^2 extrema there seems to be related to the strong average streamline curvature, which is a classical production mechanism [31]. All turbulence models studied here qualitatively agree with the experimental data, satisfactorily describing the referred trends. More precisely, the scale resolving models successfully quantify the turbulence present in the bluff body wake, substantially improving upon RANS. Furthermore, overall, the DDES hybrid model produces even more accurate solutions compared to WALE and IDDES. At the separation point ($x/D_b = 0.2$, $r/D_b = 0.5$), for instance, regarding R_{xx}/U_∞^2, DDES underestimates its peak by 12%, IDDES does so by over 30%, and WALE overestimates it by 60%. In contrast, regarding R_{rr}/U_∞^2, WALE performs better at the separation point.

Finally, RANS underestimates R_{xx}/U_∞^2 peaks by 36% and overestimates R_{rr}/U_∞^2 ones by nearly 42%.

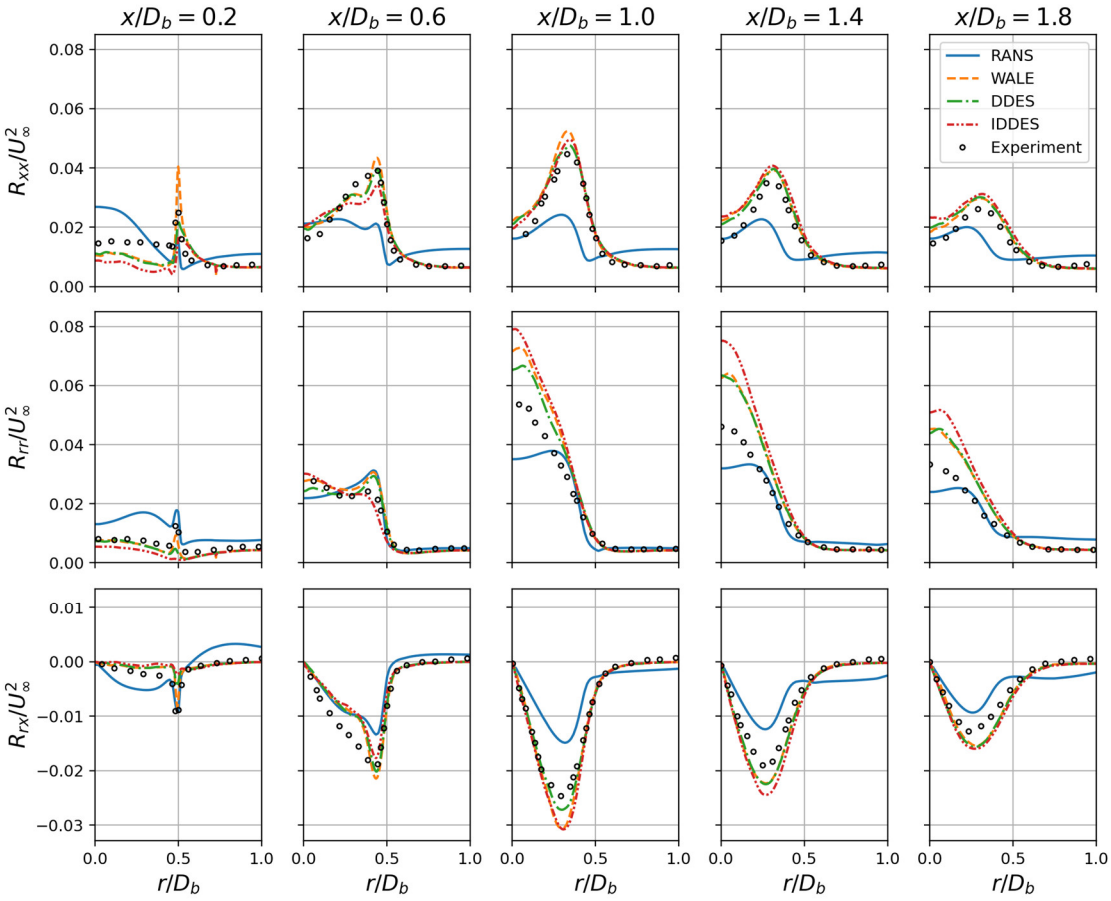

Fig. 9 Streamwise, radial Reynolds normal stresses, R_{xx}/U_∞^2 and R_{rr}/U_∞^2 respectively, and streamwise-radial shear component R_{rx}/U_∞^2. Radial profiles evaluated at five different axial positions obtained using RANS, WALE, DDES and IDDES and compared to the corresponding experimental ones. Experiments: symbols. Numerical: lines. x/D_b is the non-dimensional axial distance.

Furthermore, from Fig. 9 it may be seen that all scale resolving models show a reasonable agreement with the measured R_{xx}/U_∞^2 and R_{rr}/U_∞^2 gradients, with some minor discrepancies. In particular, at $x/D_b = 0.2$, all models describe R_{xx}/U_∞^2 as decreasing from the centerline up to its maximum value at $r/D_b = 0.5$, contradicting the radially invariant experimental behavior. Indeed, while RANS leads to results that continually decrease from $r/D_b = 0$ to $r/D_b \approx 0.5$, scale resolving approaches yield a nearly constant behavior at the centerline vicinity, starting to decrease from $r/D_b \approx 0.2$.

The streamwise-radial shear Reynolds stress R_{rx}/U_∞^2 in turn was successfully predicted by the scale resolving methods. Notice the R_{rx}/U_∞^2 extrema's position gradually moves towards the centerline as the profiles are taken further away from the bluff body. In Section 4.5, given that $b_{ij} = R_{ij}/2k$ for $i \neq j$, it will be shown that the R_{rx}/U_∞^2 results are directly related to the anisotropy tensor invariants. It is of particular importance to properly describe this turbulence property given its strong relationship with momentum transport at the bluff body wake.

The background RANS model utilized in the hybrid RANS/LES approaches could be partially responsible for the discrepancies in the results obtained using the scale resolving models. In order to illustrate the model behavior at the bluff body rim vicinity, a function returning 1 if a grid cell is in LES mode or 0 if so in RANS mode was set up when carrying out the hybrid numerical simulations. Accordingly, Fig. 10 presents the time-average values of this function at the vicinity of this flow separation point. This time-averaging yields the relative frequency spatial distribution of LES mode in the grid. It may be observed from this figure that at $r/D_b = 0.5$, for both DDES and IDDES, cells in RANS mode are found downstream the bluff body rim up to $x/D_b = 0.035$, approximately. Owing to that RANS mode implies a significantly larger turbulent viscosity than LES mode, the DDES and IDDES shear layer instabilities could be dampened by this increased viscosity in the vicinity of the bluff body. Clearly, this viscosity does not play a role in the WALE turbulence model. This may be therefore one of the reasons for the discrepancies between the maximum values of R_{xx}/U_∞^2 predicted by WALE and DDES/IDDES.

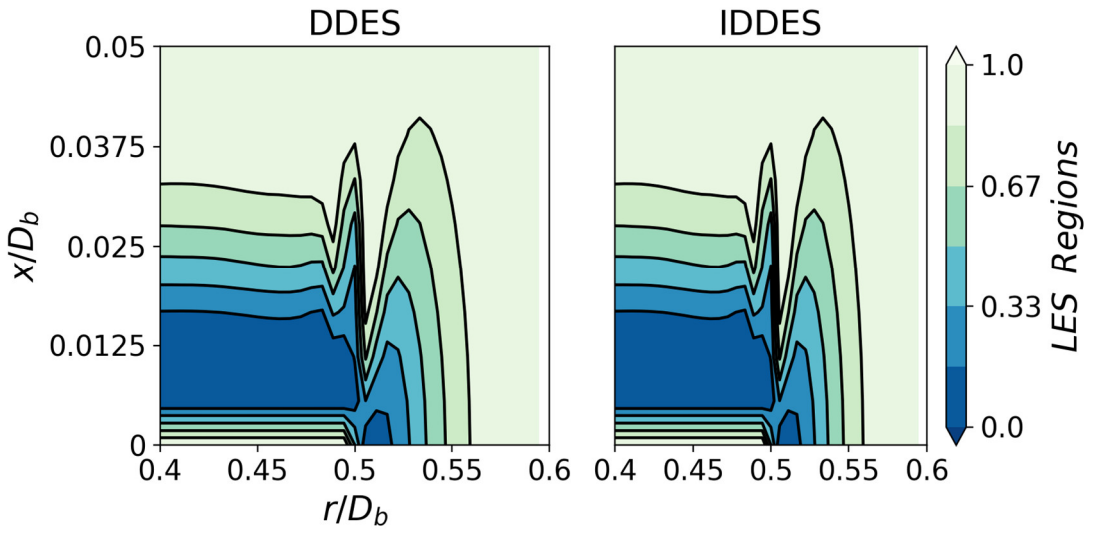

Fig. 10 Mean LES region cell indicator contours with mesh overlay characterizing DDES and IDDES results. At any given time, cell indicator returns 1 if model is in LES mode and 0 if so in RANS mode.

It is also observed from Fig. 10 that the RANS and LES regions accounted for when using the DDES and IDDES models are almost the same. This explains why both DDES and IDDES lead to boundary layers with similar thicknesses. It needs to be emphasized as well that more refined computational meshes are expected to improve the pure LES characterization of the flow instabilities under discussion, although the associated computational will also increase. The same cannot be said however for the hybrid RANS/LES approaches. This is because the delay function used in the DDES/IDDES models could be detrimental in finer meshes since it could force the model to stay in RANS mode even if the mesh could satisfactorily resolve the local flow features. This is easily verified by analyzing Eqs. (11)-(13). Observe from Eq. (12) the inverse relationship between the r_d term with the square of the distance to the nearest wall d_w^2, implying considerably high values of r_d in near-wall regions. At the limiting case indeed, when d_w approaches 0, the delay function f_d [Eq. (11)] asymptotically approaches 0 as well. As highlighted in Section 2.2.2 then, since $\tilde{d} = d_{RANS}$, the model would be forced to run in RANS mode regardless of local grid characteristics.

4.5 Turbulence anisotropy

Contours of the second (-*II*) and third (*III*) invariants of the normalized anisotropy tensor $b_{ij} = a_{ij}/2k$ are presented in 11. Here $a_{ij} = R_{ij} - \frac{2}{3}k\delta_{ij}$ represents the traceless anisotropic stress tensor, R_{ij} is the Reynolds stress tensor, k is the TKE and δ_{ij} is the Kronecker delta. These invariants are then defined as $-II = b_{ii}^2 - (b_{ii})^2$ and $III = det(b_{ij})$. It is seen from 11 that the measured $-II$ and III distributions share qualitative features. For instance, both turbulent properties' maxima are found in the shear layer and near the vortex center, whereas $-II$ and III values are significantly reduced at the vicinity of the FSMSP. More specifically, regarding the shear layer, both invariants increase downstream the bluff body rim until the FSMSP vicinity. Subsequently, both invariants continuously decrease. As noticed from 11, the RANS model predictive capabilities are most definitely lacking compared to the scale resolving turbulence models. In particular, both measured invariants reach their maximum values at the shear layer, resulting from the anisotropic behavior of the separated boundary layer. In contrast to this, the RANS calculations results indicate that the maximum anisotropy region characterizing the third invariant is located near the bluff body surface center. From the referred figure, furthermore, not only the anisotropy invariants are completely different to the experimental ones, but also the model captures no flow features within the recirculating or near wake flow regions. The lack of any anisotropic correction in RANS turbulence models could be partially responsible for this severe disagreement.

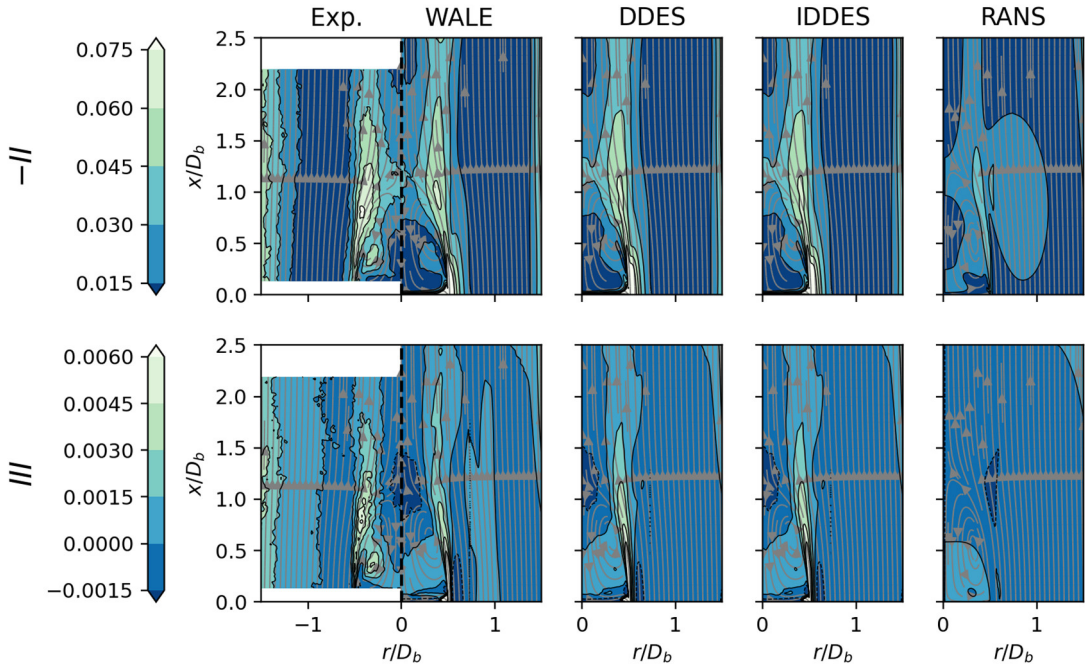

Fig. 11 Normalized anisotropy tensor second, *-II*, and third, *III*, contours of the experimental, RANS, WALE, DDES and IDDES results.

In contrast, the scale resolving turbulence approaches used here have successfully captured all major features of both invariants measured. Nevertheless, there are significant qualitative discrepancies with the reference data as none of the turbulence models predict the local $-II$ extrema measured within the recirculating flow region. More specifically, from Fig. 11 it may be observed first that both invariants' modules computed by WALE and DDES appear to be underestimated at $x/D_b = 1.0$, i.e., at the FSMSP vicinity. Table 2 summarizes in quantitative terms the deviation of each model from the extrema measured at two different locales, (i) the FSMSP vicinity and (ii) the recirculation zone. Notice that all turbulence models underestimated both $-II$ and III extrema in the FSMSP vicinity, except for IDDES which overpredicted $-II$. Within the recirculation zone, in turn, all models significantly underestimated the anisotropy. Observe that whereas WALE and DDES computed similar values, underpredicting $-II$ and III by ~56% and ~70%, respectively, IDDES deviated even further, ~71% and ~85%, respectively.

Table 2 $-II$ and III extrema observed at the vicinity of the FSMSP and within the recirculation zone.

Locale		Experiment	WALE	DDES	IDDES
FSMSP	$-\mathrm{II} \cdot 10^2$ [-]	3.19	3.06	2.97	3.89
	Deviation [%]	-	-4.08%	-6.90%	+21.9%
	$III \cdot 10^3$ [-]	-1.86	-2.06	-1.97	-2.96
	Deviation [%]	-	-10.8%	-5.91%	-59.1%
Recirculation zone	$-\mathrm{II} \cdot 10^2$ [-]	5.48	2.39	2.36	1.55
	Deviation [%]	-	-56.4%	-56.9%	-71.7%
	$III \cdot 10^3$ [-]	4.60	1.37	1.32	0.7
	Deviation [%]	-	-70.2%	-71.3%	-84.8%

In addition, the computed turbulent anisotropy magnitude at the bluff body rim separation point is larger than in the experiment. From Fig. 11 indeed, $-II$ was measured to be between 0.05 and 0.06 at the vicinity of the separation point, whereas the numerical results show that $-II \geq 0.06$. A similar behavior is found in III (11), where the maximum values were measured downstream $x/D_b = 0.25$, whereas the numerical results show that the flow separation region features the highest anisotropy. For instance, DDES predicts values higher than ~0.060 for III, while the measurements only reached ~0.006. Cruz et al. [20] point out that in high shear flow regions relative measurement uncertainties are typically of the order of 10% of the local mean velocity. Owing to the turbulent quantities discussed here are second order moments, their uncertainty is most certainly larger in these regions. Those smaller measured values could be due to the grid spacing, 1.15 mm, which is related to the minimum interrogation window size (16 x 16 px^2) that has been experimentally achieved. In order to increase the experimental resolution at this high turbulent intensity region, it would have been necessary to restrict the area of interest, which then would have led to missing the overall flow features. Therefore, the question of model and experiments comparisons in this bluff body rim region remains open.

4.6 Remarks on computational cost

The computational cost of the numerical models used in this work has been also quantified by computing the ratio between the wall time taken to complete a simulation and the physical time simulated. Therefore, its units are [Clock hours / Physical seconds]. The performance of the scale resolving techniques are compared in Table 3. The same hardware (Intel E5-2620 v4, 64 cores) was used in all simulations carried out. Due to job queueing restrictions, the complete simulations were executed over sequential jobs since they took longer than the maximum allowed time per parallel job. Hence, to make a fair comparison only the first run was considered for each scale resolving simulation. As noticed from Table 3, considering the same overall simulation conditions, the hybrid models accounted for here are computationally less expensive than pure LES approaches. RANS was not included in this analysis due to two factors. Firstly, due to the nature of the simulation a fair comparison metric was not found. Secondly, RANS simulations were not run on the same hardware. Indeed, rather cheaper and more available hardware was used for the RANS simulations since their cost is small compared to scale resolving approaches.

In addition to this slight reduction in computational cost, hybrid approaches also save cost by providing more accurate results when other aspects such as mesh resolution are accounted for. Indeed, as highlighted previously, to compute boundary layers, LES requires extremely fine meshes in near wall regions, whereas DDES and IDDES can produce reasonable results using coarser meshes. This can be verified in Fig. 6 where the LES boundary layer may be under resolved compared to DDES and IDDES (LES boundary layer thickness is slightly thinner than DDES and IDDES ones). However, it must also be mentioned that, since hybrid models may be overestimating the boundary layer thickness, further analyses of the turbulent kinetic energy spectrum are required before one can affirm whether or not LES is under resolving the boundary layer. Such an analysis is beyond the scope of the present work. Therefore, to obtain results with a pure LES approach similar to the DDES one, for instance, the computational cost would increase. This is related to both the direct cost increase associated to the increased mesh size and the associated time step decrease required to maintain numerical stability, increasing computational cost as well. Hybrid approaches seem to show therefore

potential for wider industrial use given that, while remaining more expensive than RANS techniques, its cost is not as prohibitive as that of pure LES.

Table 3 Comparison of computational performance of WALE, DDES and IDDES models.

	WALE	DDES	IDDES
Wall time [h]	119.904	119.914	119.921
Simulation time [s]	0.38713	0.40430	0.40279
Performance [h/s]	309.72	296.60	297.72

5 Conclusions

In this work, the predicting capabilities of different turbulence models were compared to existing experimental results characterizing a circular bluff body flow configuration. Three different turbulence-related approaches were studied, RANS, LES and hybrid RANS/LES. For RANS, $k\omega SST$ model was utilized. For LES in turn, the WALE SGS model was employed. Regarding RANS/LES hybrid approaches, two different models were accounted for, DDES and IDDES, both using the same background RANS model ($k\omega SST$). The turbulent flow was characterized in terms of mean velocity field, Reynolds stress tensor and flow anisotropy. The numerical results obtained using the OpenFOAM v2006 computational tool were compared with experimental measurements publicly available. Overall, the scale resolving approaches assessed here successfully captured the features of the turbulent flow, both qualitatively and quantitatively. In contrast, RANS results only agreed with the mean flow velocity measurements qualitatively but deviated significantly in quantitative terms. The RANS general trends of the stress tensor components did agree nonetheless with the measurements. Furthermore, both second and third invariants of the traceless normalized anisotropy tensor, were in complete disagreement with the experimental data. Thus, the RANS model studied here was unable to predict the measured turbulent flow anisotropy.

Scale resolving techniques exhibited a much better agreement with the experimental data. All these models determined a recirculation zone length within 1% from the measurements and the mean velocity axial component agreed with the experimental data. The bluff body boundary layer thickness was observed to have a marked effect on the flow characteristics, and more specifically on the momentum transported by the shear

layer. WALE, DDES and IDDES were observed to produce a shear layer with lower momentum content compared to RANS. Moreover, the anisotropy tensor invariants generally agreed with the experimental data. In the predictions of all scale resolving models, indeed, local anisotropy maxima were observed in the shear layer and at the vicinity of the freely standing stagnation point, likely due to the streamline curvature characterizing this region. Although turbulence anisotropy was overpredicted in the flow separation point, the scale resolving models' shear layer turbulent anisotropy largely agreed with the measurements. In addition, the studied numerical models were unable to describe the local extrema within the recirculating flow region. Finally, in computational terms, it was noticed that DDES and IDDES are slightly less expensive than LES when running under the same overall conditions. Indeed, the inclusion of a background model permits obtaining overall more accurate results with a lower resolution mesh thanks to the walls treatment involved. This is particularly important in bluff body flows because the formation of boundary layers determines their main flow features.

6 Conflict of Interest Statement

This work has been supported by CONCYTEC-FONDECYT (Peru), Contract No. 415-2019-2019-FONDECYT, "Identification of soot precursors in turbulent combustion processes through numerical modeling to reduce the impact of soot on both health and environment". During this work Luís Fernando Figueira da Silva was on leave from the Institut Pprime (CNRS - Centre National de la Recherche Scientifique, France). Support was also received by Brazil Conselho Nacional de Desenvolvimento Cientifico e Tecnologico, CNPq, under Research Grants No. 403904/2016-1 and 304444/2018-9. The authors declare that they have no conflict of interest.

7 References

1. Choi H, Jeon W-P, Kim J (2008) Control of Flow Over a Bluff Body. Annu Rev Fluid Mech 40:113–139. https://doi.org/10.1146/annurev.fluid.39.050905.110149

2. Wang G, Li Q, Liu Y (2021) IDDES method based on differential Reynolds-stress model and its application in bluff body turbulent flows. Aerosp Sci Technol 119:107207. https://doi.org/https://doi.org/10.1016/j.ast.2021.107207

3. Chen R-H, Driscoll JF, Kelly J, et al (1990) A comparison of bluff-body and swirl-stabilized flames. Combust Sci Technol 71:197–217. https://doi.org/10.1080/00102209008951632

4. AlAdawy AS, Lee JG, Abdelnabi B (2017) Effect of turbulence on NOx emission in a lean perfectly-premixed combustor. Fuel 208:160–167

5. Meraner C, Li T, Ditaranto M, Løvås T (2018) Cold flow characteristics of a novel bluff body hydrogen burner. Int J Hydrogen Energy 43:7155–7168

6. Shaddix CR, Williams TC (2017) The effect of oxygen enrichment on soot formation and thermal radiation in turbulent, non-premixed methane flames. Proc Combust Inst 36:4051–4059. https://doi.org/10.1016/j.proci.2016.06.106

7. Barlow RS (2007) Laser diagnostics and their interplay with computations to understand turbulent combustion. Proc Combust Inst 31 I:49–75. https://doi.org/10.1016/j.proci.2006.08.122

8. Köhler M, Geigle KP, Meier W, et al (2011) Sooting turbulent jet flame: Characterization and quantitative soot measurements. Appl Phys B Lasers Opt 104:409–425. https://doi.org/10.1007/s00340-011-4373-y

9. Pope SB (2000) Turbulent Flows. Cambridge University Press, Cambridge

10. Lysenko DA, Ertesvåg IS, Rian KE (2014) Large-Eddy Simulation of the Flow Over a Circular Cylinder at Reynolds Number 2 × 10^4. Flow, Turbul Combust 92:673–698. https://doi.org/10.1007/s10494-013-9509-1

11. Franco R, Celis C, Figueira da Silva LF (2019) On the Suitably of RANS Turbulence Models for Modeling Circular Bluff-Body Configurations. Proc 25th Int Congr Mech Eng. https://doi.org/10.26678/abcm.cobem2019.cob2019-1453

12. Qureshi SR, Prosser R (2007) Towards Large Eddy Simulations of a Bluff Body Burner Using an Unstructured Grid. World Congr Eng 2007 (Volume 1) 1209–1214

13. Strelets M (2001) Detached eddy simulation of massively separated flows. In: 39th AIAA Aerospace Sciences Meeting and Exhibit. pp 1–18

14. Menter FR, Kuntz M, Langtry R (2003) Ten Years of Industrial Experience with the SST Turbulence Model. Turbul Heat Mass Transf 4 4:625–632. https://doi.org/10.4028/www.scientific.net/AMR.576.60

15. Gritskevich MS, Garbaruk A V., Schütze J, Menter FR (2012) Development of DDES and IDDES formulations for the k-ω shear stress transport model. Flow, Turbul Combust 88:431–449. https://doi.org/10.1007/s10494-011-9378-4

16. Spalart PR (2009) Detached-Eddy Simulation. Annu Rev Fluid Mech 41:181–202. https://doi.org/10.1146/annurev.fluid.010908.165130

17. Spalart PR, Deck S, Shur ML, et al (2006) A new version of detached-eddy simulation, resistant to ambiguous grid densities. Theor Comput Fluid Dyn 20:181–195. https://doi.org/10.1007/s00162-006-0015-0

18. OpenCFD OpenFOAM® - Official home of The Open Source Computational Fluid Dynamics (CFD) Toolbox. https://www.openfoam.com/. Accessed 20 Jul 2019

19. Nicoud F, Ducros F (1999) Subgrid-Scale Stress Modelling Based on the Square of the Velocity Gradient Tensor. Flow, Turbul Combust 62:183–200. https://doi.org/10.1023/A:1009995426001

20. Cruz Villanueva JJ, Figueira da Silva LF (2016) Study of the Turbulent Velocity Field in the Near Wake of a Bluff Body. Flow, Turbul Combust 97:715–728. https://doi.org/10.1007/s10494-016-9709-6

21. Valencia S, Ruiz S, Manrique J, et al (2021) Soot modeling in turbulent diffusion flames: review and prospects. J Brazilian Soc Mech Sci Eng 43:219. https://doi.org/10.1007/s40430-021-02876-y

22. Lysenko DA, Ertesvåg IS, Rian KE (2012) Large-eddy simulation of the flow over a circular cylinder at Reynolds number 3900 using the openfoam toolbox. Flow, Turbul Combust 89:491–518. https://doi.org/10.1007/s10494-012-9405-0

23. Moukalled F, Mangani L, Darwish M (2016) The Finite Volume Method in Computational Fluid Dynamics: An Advanced Introduction with OpenFOAM® and Matlab®

24. Pope SB (2004) Ten questions concerning the large-eddy simulation of turbulent flows. New J Phys 6:35. https://doi.org/10.1088/1367-2630/6/1/035

25. Spalart PR, Jou WH, Strelets MK, Allmaras SR (1997) Comments on the feasibility of LES for wings and on a hybrid RANS/LES approach. Adv DNS/LES 1:4–8

26. Issa RI (1986) Solution of the implicitly discretised fluid flow equations by operator-splitting. J Comput Phys 62:40–65. https://doi.org/https://doi.org/10.1016/0021-9991(86)90099-9

27. Robertson E, Choudhury V, Bhushan S, Walters DK (2015) Validation of OpenFOAM numerical methods and turbulence models for incompressible bluff body flows. Comput Fluids 123:122–145. https://doi.org/10.1016/j.compfluid.2015.09.010

28. Wurps H, Steinfeld G, Heinz S (2020) Grid-Resolution Requirements for Large-Eddy Simulations of the Atmospheric Boundary Layer. Boundary-Layer Meteorol 175:179–201. https://doi.org/10.1007/s10546-020-00504-1

29. Davidson L (2009) Large Eddy Simulations: How to evaluate resolution. Int J Heat Fluid Flow 30:1016–1025. https://doi.org/10.1016/j.ijheatfluidflow.2009.06.006

30. Poletto R, Craft T, Revell A (2013) A new divergence free synthetic eddy method for the reproduction of inlet flow conditions for LES. Flow, Turbul Combust 91:519–539. https://doi.org/10.1007/s10494-013-9488-2

31. Durbin PA, Petersson Reiff BA (2010) Statistical Theory and Modeling for Turbulent Flows